crystals

MDPI

Article

Rheological Solidification Behavior and Mechanical Properties of AZ91-Sn Alloys

Di Tie [1], Boyu Zhang [1], Lufei Yan [1], Renguo Guan [2,*], Zhaoshan Ji [3], Haifeng Liu [4], Deliang Zhang [1], Debao Liu [5] and Minfang Chen [5]

[1] Key Laboratory of Lightweight Structural Materials Liaoning Province, School of Materials Science and Engineering, Northeastern University, Shenyang 110819, China; tie-di@hotmail.com (D.T.); boyuzhang@neu.edu.cn (B.Z.); lufeiyan@neu.edu.cn (L.Y.); zhangdl@mail.neu.edu.cn (D.Z.)

[2] School of Materials Science and Engineering, Northwestern Polytechnical University, Xi'an 710072, China

[3] Hubei Province Key Laboratory of Advanced Welding Technology, Xiaogan 432000, China; zhaoshanji@neu.edu.cn

[4] Prospective Technology Department, The CITIC Dicastal Institute, Qinhuangdao 066011, China; haifeng.liu@citic.com

[5] School of Materials Science and Engineering, Tianjin University of Technology, Tianjin 300384, China; debaoliu@tut.cn (D.L.); chenminfang@tut.cn (M.C.)

* Correspondence: guanrg@mail.neu.edu.cn; Tel.: +86-24-83681990

Received: 11 November 2019; Accepted: 25 November 2019; Published: 3 December 2019

check for updates

Abstract: The solidification and tensile deformation behaviors of rheo-cast AZ91-Sn alloys were revealed to study the effects of Sn alloying on improvement of AZ91 alloy's mechanical properties. Two kinds of $Mg_{17}Al_{12}$ phases precipitated from the supersaturated magnesium matrix during rheo-solidification were observed: coarse discontinuous precipitates (DP) at grain boundaries and small-sized continuous precipitates (CP) inside grains. With increasing Sn content, the amount of $Mg_{17}Al_{12}$ phases was increased whilst the amount of Al atoms in the matrix was decreased. Due to the higher melting point of Mg_2Sn than $Mg_{17}Al_{12}$, Mg_2Sn precipitated earlier from the melt, and therefore provided heterogeneous nuclei for $Mg_{17}Al_{12}$ during the eutectic reaction. Due to grain refinement and solid solution strengthening, AZ91-2.4Sn (mass%) gained 52% increase in tensile strength and 93% increase in elongation compared with pure AZ91 alloy. The higher-density twins and microcracks induced by Sn alloying relaxed stress concentration during plastic deformation, so the fracture mode was transformed from cleavage fracture of pure AZ91 alloy to ductile fracture of AZ91-Sn alloys.

Keywords: rheo-cast; solidification; AZ91 alloy; stannum; mechanical properties

1. Introduction

Global warming is becoming one of the most serious environmental problems in recent years, and automobile manufacturers worldwide are making efforts to meet the rising environmental regulations and product standards [1,2]. Therefore, lightweight car body designs to satisfy the fuel economy and emission control standards for automobiles have been gaining increasing attentions [3–5]. As one of the lightest metallic structural metal with high specific strength and stiffness, magnesium alloys have been widely applied in automobile industry [6]. Among hundreds of commercial magnesium alloys, AZ91 alloy is the most extensively used casting alloy for its excellent casting performance and balanced mechanical properties [7]. However, the ductility of AZ91 alloy still needs to be improved to meet the manufacture of thin-wall parts, which limits AZ alloys' applications [8,9]. The main reason for lower ductility is the continuous network of the $Mg_{17}Al_{12}$ phase along the grain boundaries in AZ91 alloy matrix. Many studies have been conducted in the past few years to improve the microstructural stability of AZ91 by alloying or micro-alloying [10,11]. The main purpose of these studies was to suppress the formation of the $Mg_{17}Al_{12}$ phase or create more thermally stable precipitates. Alloying elements, such as Zr and rare earth elements, having high affinity for Al, can significantly reduce the amount of $Mg_{17}Al_{12}$ by consuming the aluminum content in the alloy to form the Al-containing intermetallic compounds including Al_3Zr_2, Al_2Zr, and $Al_{11}RE_3$ with higher melting points [12,13]. Although these elements improve the creep resistance and suppress the discontinuous precipitation of the secondary $Mg_{17}Al_{12}$ phases during heat treatment, they could hardly change the volume fraction of $Mg_{17}Al_{12}$ in cast conditions [14].

Sn alloying has been proved an effective method for grain refinement and ductility improvement or AZ91 alloys in previous studies [15,16]. Magnesium matrix can be evidently refined by adding appropriate Sn content, because Sn content results in formation of Mg_2Sn precipitates in the inter-dendritic region during solidification, which could effectively suppress the discontinuous $Mg_{17}Al_{12}$ precipitation [17]. The melting point of Mg_2Sn phase is 770 °C, which is higher than that of the $Mg_{17}Al_{12}$ phase in AZ91 alloy. Mg_2Sn precipitates earlier from the melt during solidification process, and therefore could provide heterogeneous nuclei for $Mg_{17}Al_{12}$ in eutectic reaction. Kim et al. studied the solidification behavior of AZ91−xSn alloy (x = 1, 3, 5, mass%) and found that addition of Sn led to suppression of the discontinuous precipitation as well as significant improvement of hardness and strength [18]. However, Li's study showed that the hardness decreased with increasing Sn content from 0.5 to 1 mass%. Therefore, the aim of the present study is to investigate the effect of Sn addition between 0.8 and 2.4 mass% on the rheo-solidification behavior and mechanical properties of AZ91 alloy [19]. The effect of semi-solid rheo-casting process on AZ91-Sn alloys microstructure revolution is also thoroughly studied for its potential of improving mechanical properties especially ductility. Rheo-forming is one of the promising semi-solid metal processing technologies for producing high-performance AZ alloys [20]. During rheo-forming, alloys are isothermally treated between solidus and liquidus temperature, and the primary dendritic microstructure transforms into globular structure leading to improved mechanical properties especially ductility [21]. H. Watari has studied semisolid AZ31B magnesium alloy processed by rheo-forming, via which alloy sheets with a thickness of 2.5 mm were obtained [22]. Guan et al. have successfully prepared AZ magnesium alloy sheets with improved mechanical properties by rheo-rolling [23]. Therefore, the aim of this work was to investigate the effects of Sn addition on the solidification behavior during rheo-casting and the mechanical properties of rheo-cast AZ91-Sn alloys. Scanning electron microscopy, energy-dispersive analysis, high-resolution transmission electron microscopy, etc. were used to analyze the rheological solidification behavior of AZ91-Sn alloys, and the alloys' fracture behavior was also revealed via tensile tests and fractography analysis.

2. Materials and Methods

The experimental materials were AZ91 with x mass% Sn content (x = 0.8, 1.6, and 2.4), and the alloys are named AZ91-0.8Sn, AZ91-1.6Sn, and AZ91-2.4Sn in this paper, respectively. The alloys were prepared in an electrical resistance furnace (HLJ-10-12, Hengli, Luoyang, China) under a mixture of an SF_6 and CO_2 protective gas atmosphere. Before rheo-casting, the surface of the crucible and accessory devices (pressing cover, slag scoop, etc.) were washed successively by chromic acid and deionized water and dried in a vacuum drier (FZG-20, Shenwei Co., Nanjing, China). The semi-solid slurry was prepared by a rheologic treatment device with vibration equipment, which was designed and manufactured by our research team (Figure 1) [24]. The processing parameters were as follows: casting temperature from 670 to 690 °C, casting speed of 0.052 m/s, and vibration frequency of 80 Hz. The casting temperature was within the semi-solid temperature range of AZ91 alloy, in which the melt could be rheo-solidified. When the melt touched the sloping plate, the melt was cooled rapidly. Therefore, heterogeneous nucleation formed on the surface of the sloping plate under large undercooling. Under the vibration and shear field, the nucleus ceaselessly fell off from the surface, which led to grain spheroidization and refinement during the rapid solidification.

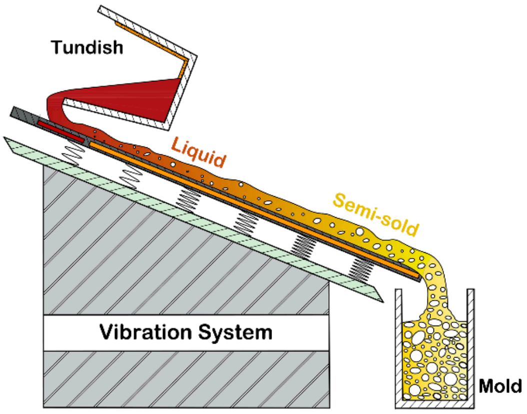

Figure 1. The schematic diagram of the semi-solid rheo-casting process.

The prepared samples were polished and etched by the solution of 15 mL HCl + 45 mL C_2H_5OH + 40 mL H_2O. A metallographic microscope (GX51; Olympus, Japan) was used to observe the microstructure, and a scanning electron microscope (SEM, SSX-550; Shimadzu, Japan) equipped with an energy-dispersive (EDS) was used for precipitate identification and fractography analysis. In preparation for high-resolution transmission electron microscopy (HR-TEM) analysis, the polished specimens were thinned by ion sputtering and observed using a Tecnai G2 (FEI Company, Eindhoven, The Netherlands) at 200 kV for phase identification. An electronic tensile testing machine (CMT5305; MST, China) was used to test the mechanical properties of the alloy samples, and the tensile speed was set as 3 mm/min. The size of the tensile sample is shown in Figure 2. All the tests were carried out in five-duplicates, and the data were expressed as mean ± standard deviation (SD).

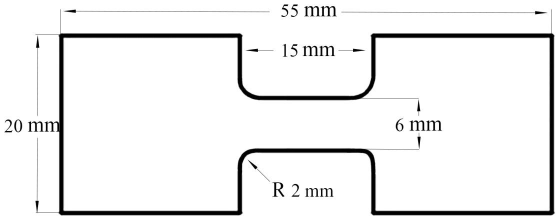

Figure 2. The scheme and dimensions of the samples for tensile tests.

3. Results and Discussion

Primary α-Mg matrix solidified first on the surface of the sloping plate due to the water-cooling system under the plate, and the shearing vibration equipment led to dynamical non-equilibrium solidification. The semi-solid slurry composed of primary α-Mg and melt rich in Al at the end of the sloping plate. The alloy matrix was mainly composed of spherical equiaxed grains in the size from ca. 30 μm in AZ91-0.8Sn alloy to ca. 20 μm in AZ91-2.4Sn alloy. Based on SEM micrographs and EDS results (Figure 3), it is evident that both the coarse discontinuous $Mg_{17}Al_{12}$ precipitate (DP) and the small-sized continuous $Mg_{17}Al_{12}$ precipitate (CP) were produced during the semi-solid casting process [17].

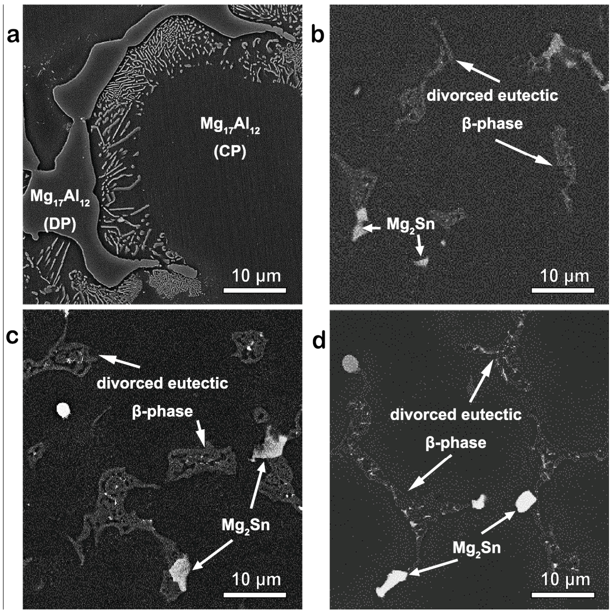

Figure 3. SEM images of rheo-cast AZ91 and AZ91-Sn alloys: (**a**) pure AZ91; (**b**) AZ91-0.8Sn; (**c**) AZ91-1.6Sn; and (**d**) AZ91-2.4Sn; both the coarse discontinuous $Mg_{17}Al_{12}$ precipitate (DP) and the small-sized continuous $Mg_{17}Al_{12}$ precipitate (CP) were produced during the semi-solid casting process.

The coarse DP inhomogeneously distributed at the grain boundary, while the much smaller CP uniformly distributed inside grain. With increasing Sn content, the precipitation of $Mg_{17}Al_{12}$ phase was improved whilst the amount of Al atoms in the matrix was reduced [18]. The Mg_2Sn precipitate was always accompanied by the divorced eutectic β-phase (Figure 3). Due to the higher melting point of Mg_2Sn phase than $Mg_{17}Al_{12}$, Mg_2Sn precipitated earlier from the melt. Therefore, Mg_2Sn precipitate provided heterogeneous nuclei for $Mg_{17}Al_{12}$ during the eutectic reaction.

Surface EDS maps of the AZ91-0.8Sn alloy was shown in Figure 4. The distribution of Al elements was mainly at the grain boundary zone in Mg matrix. Most of the Al atoms reacted with Mg atoms to form a binary intermetallic compound, whilst a small portion dissolved in the matrix. Elemental Sn mainly distributed at the grain boundary together with Al element, which was found more in Mg rich zone and less in Al rich zone (Figure 4). The EDS analysis upon higher magnification SEM images showed a large number of small-sized Mg_2Sn precipitate formed during rheo-cast process (Figure 5a,b). This kind of Mg_2Sn phase's size was ca. 3–5 µm, and also accompanied by divorced eutectic β-phase distributed at grain boundary similar to the Mg_2Sn precipitate (Figure 3). Figure 5c shows the HR-TEM image of AZ91-0.8Sn alloy, in which a small-sized Mg_2Sn precipitate was marked by a cross. The selected electron diffraction pattern in Figure 5c obtained from the region marked by the cross was indexed as a [111] zone of face-centered cubic (fcc) Mg2Sn. The results show that Mg_2Sn precipitate formed together with eutectic β-phase during solidification, and these intermetallic compounds with high melting point became heterogeneous precipitate nuclei and refined the alloy matrix during solidification process.

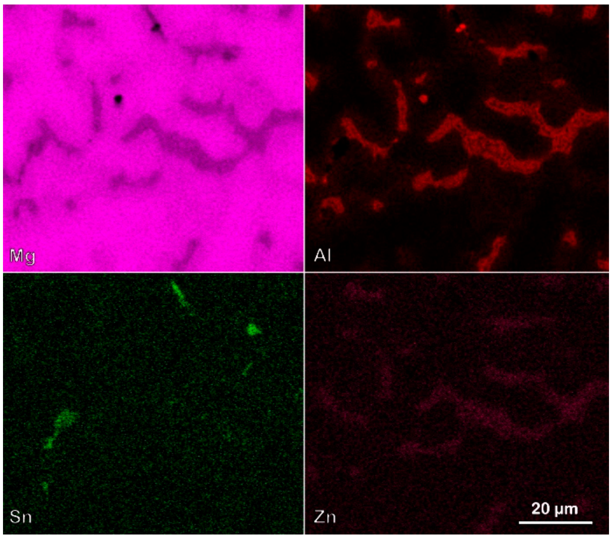

Figure 4. Surface energy dispersive (EDS) maps of AZ91-0.8Sn alloy.

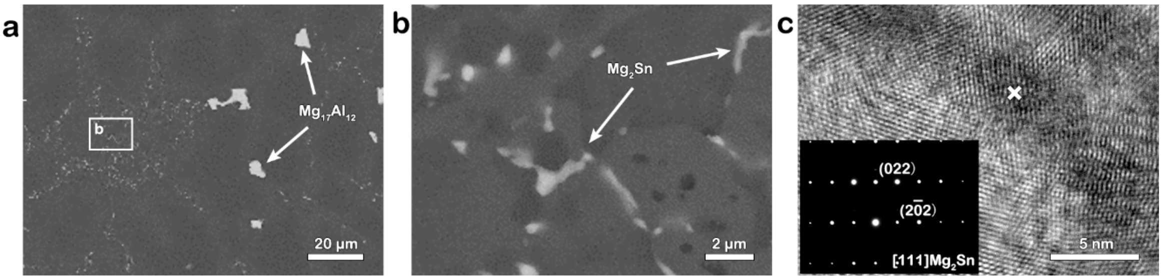

Figure 5. The SEM image (**a**) and the local map in higher magnification of the framed area (**b**) and high-resolution (HR)-TEM image (**c**) of AZ91-0.8Sn alloy; the selected electron diffraction pattern obtained from the region marked by the cross in Figure 5c.

During AZ91 alloy rheo-solidification process, the α-Mg matrix was preferentially formed as solid phases. The residual liquid phase underwent eutectic reaction when the temperature dropped to the eutectic temperature due to non-equilibrium solidification. The left β-phase distributed at grain boundary and formed divorced eutectic phases. Addition of Sn in AZ91 alloy led to significant grain refinement. When the Sn content was 0.8 mass%, small-sized DP was the dominant type of $Mg_{17}Al_{12}$ precipitate. The Sn content enriched at grain boundary or dendrite as shown in Figure 3, due to the low solid solubility of Sn in Mg (ca. 0.45 mass% at 200 °C). The solid solubility of Sn in Mg decreased sharply with decreasing temperature. As a result, Sn atoms enriched along the solid–liquid interface and precipitated in undercooled condition. When dendrite grew in undercooled regions in Mg-Al-Sn ternary alloy system, the criterion of constitutional undercooling can be deduced as follows [25]:

$$\frac{G}{R} \ll -\frac{m_{Al}C_{\circ}^{Al}1 - K_{Al}}{K_{Al}D_{Al}} - \frac{m_{Sn}C_{\circ}^{Sn}(1 - K_{Sn})}{K_{Sn}D_{Sn}}, \tag{1}$$

where G is the temperature gradient at the solid-liquid interface; R is the grain growth rate; m_{Al} is the slope of the liquid surface when the Al content is $C_{\circ}^{Al}$; m_{Sn} is the slope of the liquid surface when the Sn content is $C_{\circ}^{Sn}$; K_{Al} and K_{Sn} are the equilibrium partition coefficients of Al and Sn, respectively; and D_{Al} and D_{Sn} are the equilibrium diffusion coefficients of Al and Sn, respectively. Considering the two equations below can be introduced:

$$\Delta T_{\circ}^{Al} = -\frac{m_{Al}C_{\circ}^{Al}(1 - K_{Al})}{K_{Al}}, \tag{2}$$

$$\Delta T_{\circ}^{Sn} = -\frac{m_{Sn} C_{\circ}^{Sn} (1 - K_{Sn})}{K_{Sn}}, \tag{3}$$

where $\Delta T_{\circ}^{Al}$ represents the temperature difference between liquidus and solidus of Al-rich region in Mg-Al-Sn system; and $\Delta T_{\circ}^{Sn}$ represents the temperature difference between liquidus and solidus of Sn-rich region in Mg-Al-Sn system. Combining Equations (2) and (3) with Equation (1), the following equation can be obtained:

$$\frac{G}{R} \leq \frac{\Delta T_{\circ}^{Al}}{D_{Al}} + \frac{\Delta T_{\circ}^{Sn}}{D_{Sn}}. \tag{4}$$

It can be concluded that when G/R and Al content are constants as in this study, $C_{\circ}^{Sn}$ and $\Delta T_{\circ}^{Sn}$ increase with increasing Sn content. This effect will lead to constitutional undercooling of the alloy, which could accelerate formation of dendrite. The solid solubility of Sn in Mg decreased sharply with decreasing temperature during solidification process, so Sn was enriched at grain boundaries or dendrites at the end of the solidification process (Figure 3). Mg_2Sn has bcc (body-centered cubic) structure while $Mg_{17}Al_{12}$ has fcc (face-centered cubic) structure. The experimental results showed Mg_2Sn phase was mostly accompanied by the $Mg_{17}Al_{12}$ phase, which indicated that the Mg_2Sn phase provided heterogeneous points during $Mg_{17}Al_{12}$ phase precipitation. Thus, more $Mg_{17}Al_{12}$ phases were formed with increasing Sn content. Some previous studies have accurately determined the habit plane between Mg_2Sn and $Mg_{17}Al_{12}$ phase [26]. The existence of the habit plane $(220)_{Mg2Sn}$ $//(330)_{Mg17Al12}$ made Mg_2Sn become the heterogeneous nucleation point of $Mg_{17}Al_{12}$ [27]. In our study, the α-Mg matrix solidified first during the solidification process. With decreasing temperature, the rapid decrease of Sn solid solubility in Mg matrix led to the enrichment of Sn at the solid–liquid interface so that Mg_2Sn phase was formed by eutectic reaction: $L \rightarrow \alpha\text{-}Mg + Mg_2Sn$. With ongoing solidification, the (330) surface of $Mg_{17}Al_{12}$ phase nucleated and grew along the (220) surface of Mg_2Sn phase. The reaction formation formula is as follows: $L \rightarrow \alpha\text{-}Mg + Mg_{17}Al_{12} + Mg_2Sn$ [28]. The model of solidification process can be depicted in Figure 6.

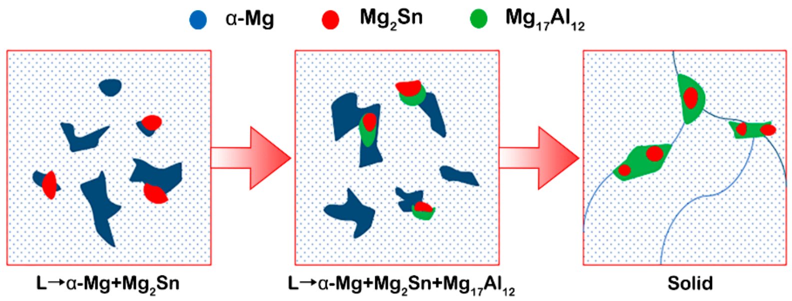

Figure 6. The schematic diagram of AZ91-Sn alloy solidification behavior.

The tensile strength and elongation of AZ91 and AZ91-Sn alloys were shown in Figure 7. The tensile strength of AZ91 alloy was 143.2 ± 2.2 MPa and the elongation was 4.21% ± 0.16%. When 0.8 mass% Sn was added, the tensile strength of the alloy increased to 156.1 ± 3.2 MPa, and the elongation increased to 6.61% ± 0.15%. AZ91-2.4Sn showed the highest tensile strength of 217.0 ± 2.3 MPa, as well as the highest elongation of 8.11% ± 0.18%. Compared with pure AZ91 alloy, AZ91-2.4Sn gained 52% increase in tensile strength and 93% increase in elongation. Grain refinement was proved an efficient method to improve both strength and ductility of magnesium alloys, and alloying is one of the most common used grain refinement methods. The grain size of AZ91-Sn alloys was much smaller than that of pure AZ91 alloy (Figure 3). Therefore, the addition of Sn not only induced precipitation strengthening but also led to grain refinement strengthening in the present study. Furthermore, due to higher grain density by the grain refinement, deformation could be dispersed in more grains when stress applied. The difference of strain between deformed grains became more homogeneous, which led to more uniform deformation and improved the ductility. The three AZ91-Sn alloys had similar grain size and Sn content in Mg matrix (ca. 0.45 mass% at 200 °C), so they had similar effect of grain refinement strengthening and solid solution strengthening. Therefore, AZ91-2.4Sn alloy exhibited the highest tensile strength and elongation due to its highest Sn content, which led to more evident precipitation strengthening.

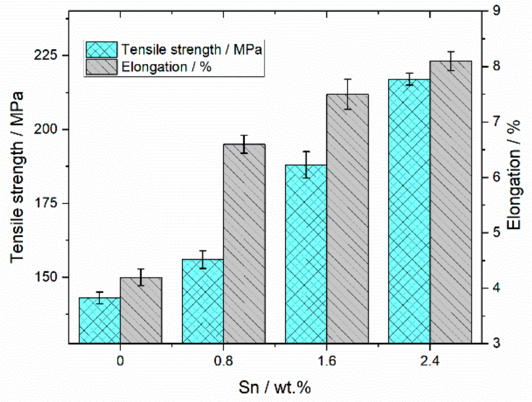

Figure 7. The tensile strength and elongation of AZ91 and AZ91-Sn alloys.

The tensile fracture SEM morphology of pure AZ91 and AZ91-Sn alloys are shown in Figure 8. River patterns with cleavage plans were the dominant fracture morphology of pure AZ91 (Figure 8a), which means the absorbed energy of plastic deformation was very low. The evident river patterns were composed of a large number of tearing edges and cleavage steps, so the fracture type of pure AZ91 can be classified as cleavage fracture. Compared with pure AZ91, the fracture surface of AZ91-Sn alloys presented more dimples, and less quasi-cleavage planes, which could be characterized by the ductile fracture [29]. The fracture surface is composed of a small plane of quasi-cleavage and a mixture of micropores and tear ridges. The river patterns in AZ91-Sn alloys' fracture morphology were short and curved, indicating that the fracture mode was transformed from cleavage fracture to ductile fracture. With increasing Sn content, the density of dimples evidently increased (Figure 8b–d). The finer recrystallized grains due to higher Sn content could effectively hinder the nucleation and propagation of cleavage cracks, so the AZ91-2.4Sn exhibited the highest elongation with the least cleavage plane density on fracture surface [30].

From the SEM images of the longitudinal section of tensile fracture (Figure 9), it can be concluded that the pure AZ91 alloy began to fracture from the interface between coarse $Mg_{17}Al_{12}$ DPs and matrix. The fracture then grew and propagated along grain boundaries, leading to intergranular fracture [31]. Unlike pure AZ91's fracture morphology, more twins and microcracks could be observed in AZ91-Sn alloys' longitudinal section (as the circled areas in Figure 9b–d). Sn addition facilitated improving tensile strength by refining matrix and forming finer precipitates with different orientations. The refined grains could effectively hinder the nucleation and propagation of cleavage cracks, so that AZ91-Sn alloys fractured by connecting the microcracks around $Mg_{17}Al_{12}$ CPs inside the grain rather than $Mg_{17}Al_{12}$ DPs at the grain boundary [8]. Furthermore, higher-density twins and microcracks induced by Sn alloying could relax stress concentration during plastic deformation [31]. Therefore, the AZ91-Sn alloys could withstand higher load and lager deformation with increasing Sn content. The fracture results also prove that the addition of Sn can evidently improve the ductility of AZ91 magnesium alloy. This improvement in ductility is crucial to magnesium structural parts for industrial applications, especially the manufacture of thin-wall automotive parts. Our future study will focus on the effect of higher Sn content addition on the precipitation behavior during heat treatment, especially the thermal stability of Mg_2Sn precipitates.

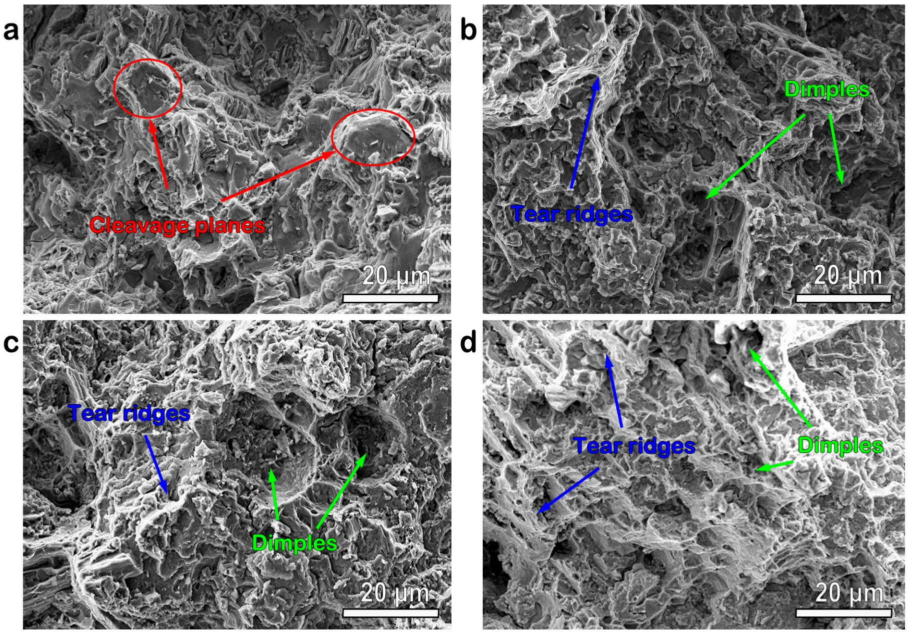

Figure 8. Representative SEM images showing the surface fracture morphology of: (**a**) pure AZ91; (**b**) AZ91-0.8Sn; (**c**) AZ91-1.6Sn; and (**d**) AZ91-2.4Sn.

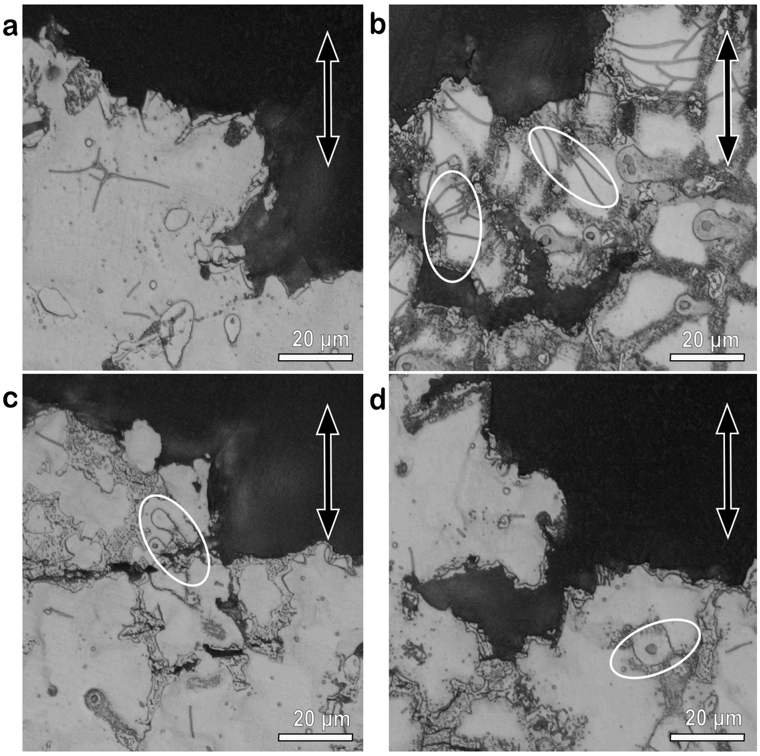

Figure 9. Tensile fracture morphology of longitudinal sections of: (**a**) pure AZ91; (**b**) AZ91-0.8Sn; (**c**) AZ91-1.6Sn; and (**d**) AZ91-2.4Sn; the load direction is marked by a double arrowhead in each image.

4. Conclusions

The effects of Sn addition on the solidification behavior during rheo-casting and the mechanical properties of the rheo-cast AZ91-Sn alloys were investigated in this work, and the following essential conclusions were obtained:

(1) The rheo-cast AZ91-Sn alloys were mainly composed of spherical equiaxed grains in the size from ca. 30 µm in AZ91-0.8Sn alloy to ca. 20 µm in AZ91-2.4Sn alloy. Coarse DPs at grain boundaries and small-sized CPs inside grains were formed during rheo-solidification process. Mg_2Sn precipitated earlier from the melt, and therefore provided heterogeneous nuclei for $Mg_{17}Al_{12}$ during the eutectic reaction.

(2) The addition of Sn effectively refined both the alloy matrix and the DPs, due to which AZ91-2.4Sn showed the highest tensile strength of 217.0 ± 2.3 MPa, as well as the highest elongation of 8.11% ± 0.18%. Compared with pure AZ91 alloy, AZ91-2.4Sn gained 52% increase in tensile strength and 93% increase in elongation.

(3) The fracture mode was gradually transformed from cleavage fracture to ductile fracture with increasing Sn content in the alloy.

Author Contributions: Conceptualization, D.T.; methodology, B.Z. and L.Y.; formal analysis, Z.J.; data curation, D.L. and H.L.; writing—original draft preparation, D.T.; writing—review and editing, M.C. and R.G.; supervision, R.G. and D.Z.

Funding: This research was funded by National Natural Science Foundation of China, grant numbers 51771045, U1764254, and 51974083.

Acknowledgments: The authors wish to thank Lizhong Liu and Fengguo Liu for their kind help in the laboratory. Shenyang Ligong University is sincerely acknowledged for providing experimental instruments.

Conflicts of Interest: The authors declare no conflict of interest.

References

1. Jin, P.K.; Gu, Y.G.; Shi, X.; Yang, W.N. Non-negligible greenhouse gases from urban sewer system. *Biotechnol. Biofuels* **2019**, *12*, 100. [CrossRef] [PubMed]
2. Ding, S.; Liu, Y. Adsorption of CO_2 from flue gas by novel seaweed-based koh-activated porous biochars. *Fuel* **2020**, *260*, 116382. [CrossRef]
3. Zhang, J.-l.; Liu, Y.-l.; Liu, J.; Yu, Y.-c.; Wang, S.-b. The effect of Gd element and solution treatment on the microstructure of AZ31 magnesium alloy and its kinetic model. *J. Alloys Compd.* **2016**, *663*, 610–616. [CrossRef]
4. Liu, P.; Jiang, H.; Cai, Z.; Kang, Q.; Zhang, Y. The effect of Y, Ce and Gd on texture, recrystallization and mechanical property of Mg–Zn alloys. *J. Magnes. Alloys* **2016**, *4*, 188–196. [CrossRef]
5. Bu, F.; Yang, Q.; Qiu, X.; Zheng, T.; Zhang, D.; Niu, X.; Li, Y.; Liu, X.; Meng, J. Study on the assemblage of Y and Gd on microstructure and mechanical properties of hot extruded Mg-Al-Zn alloy. *Mater. Sci. Eng. A* **2015**, *639*, 198–207. [CrossRef]
6. Yoo, M.; Song, J.; Oh, J.; Kang, S.; Kim, K.; Yang, S.; Moon, M. Development of a bus armrest fabrication process with a high-vacuum, high-pressure die-casting process using the AM60 alloy. *Robot. Comput. Int. Manuf.* **2019**, *55*, 154–159. [CrossRef]
7. Mehr, N.F.; Aashuri, H. The effects of annular electromagnetic stirring parameters on microstructure evolution of rheocast AZ91 magnesium alloy. *J. Mater. Res. Technol.* **2019**, *8*, 2300–2308. [CrossRef]
8. Turen, Y. Effect of Sn addition on microstructure, mechanical and casting properties of AZ91 alloy. *Mater. Des.* **2013**, *49*, 1009–1015. [CrossRef]
9. Chalasani, D.; Jain, M.K.; Shankar, S.; FAZeli, F. Workability characteristics and deformation mechanisms of die-cast AM60 and AZ91 magnesium alloys: Correlation with processing maps. *J. Mater. Eng. Perform.* **2018**, *28*, 123–139. [CrossRef]
10. Cai, H.S.; Guo, F.; Su, J.; Liu, L. Existing forms of Gd in AZ91 magnesium alloy and its effects on mechanical properties. *Mater. Res. Express* **2019**, *6*, 066541. [CrossRef]
11. Li, N.; Yan, H. The effects of rare earth Pr and heat treatment on the wear properties of AZ91 alloy. *Crystals* **2018**, *8*, 256. [CrossRef]
12. Kabirian, F.; Mahmudi, R. Effects of Zr additions on the microstructure and impression creep behavior of AZ91 magnesium alloy. *Metall. Mater. Trans. A* **2010**, *41*, 3488–3498. [CrossRef]
13. Mahmudi, R.; Kabirian, F.; Nematollahi, Z. Microstructural stability and high-temperature mechanical properties of AZ91 and AZ91 + 2RE magnesium alloys. *Mater. Des.* **2011**, *32*, 2583–2589. [CrossRef]

14. Mahmudi, R.; Moeendarbari, S. Effects of Sn additions on the microstructure and impression creep behavior of AZ91 magnesium alloy. *Mater. Sci. Eng. A* **2013**, *566*, 30–39. [CrossRef]
15. Boby, A.; Srinivasan, A.; Pillai, U.T.S.; Pai, B.C. Mechanical characterization and corrosion behavior of newly designed Sn and Y added AZ91 alloy. *Mater. Des.* **2015**, *88*, 871–879. [CrossRef]
16. Sedighi, O.; Shabestari, S.G.; Yavari, F. Investigation on the effect of Sn on solidification and microstructure of AZ91 magnesium alloy using cooling curve thermal analysis. *Thermochim. Acta* **2018**, *667*, 165–172. [CrossRef]
17. Lin, H.; Yang, M.B.; Tang, H.; Pan, F.S. Effect of minor Sc on the microstructure and mechanical properties of AZ91 magnesium alloy. *Prog. Nat. Sci. Mater.* **2018**, *28*, 66–73. [CrossRef]
18. Kim, J.K.; Oh, S.H.; Kim, K.C.; Kim, W.T.; Kim, D.H. Effect of Sn addition on the precipitation behavior in AZ91 magnesium alloy. *Mater. Trans.* **2017**, *58*, 963–966. [CrossRef]
19. Li, R.G.; Xu, Y.; Qi, W.; An, J.; Lu, Y.; Cao, Z.Y.; Liu, Y.B. Effect of Sn on the microstructure and compressive deformation behavior of the AZ91d aging alloy. *Mater. Charact.* **2008**, *59*, 1643–1649. [CrossRef]
20. Nami, B.; Shabestari, S.G.; Razavi, H.; Mirdamadi, S.; Miresmaeili, S.M. Effect of Ca, REe elements and semi-solid processing on the microstructure and creep properties of AZ91 alloy. *Mater. Sci. Eng. A* **2011**, *528*, 1261–1267. [CrossRef]
21. Yan, F.; Sun, L.; Gong, Y.; Hao, Y. Steady state rheological characteristic of semisolid magnesium alloy. *J. Mater. Sci. Technol.* **2007**, *23*, 637–640.
22. Watari, H.; Davey, K.; Rasgado, M.T.; Haga, T.; Izawa, S. Semi-solid manufacturing process of magnesium alloys by twin-roll casting. *J. Mater. Process. Technol.* **2004**, *155*, 1662–1667. [CrossRef]
23. Guan, R.; Zhang, Q.; Dai, C.; Zhao, Z.; Liu, C. Simulation and optimization of thermal field during continuous constrained rheo-rolling of AZ31 alloy. *Acta Metall. Sin.* **2011**, *47*, 1167–1173.
24. Guan, R.; Tie, D.; Li, Z.; An, Y.; Wang, X.; Li, Q.; Chen, X. Microstructure evolution and mechanical property improvement of aluminum alloys with high magnesium content during continuous rheo-extrusion. *Mater. Sci. Eng. A* **2018**, *738*, 31–37. [CrossRef]
25. Hu, H. *Principle of Metal Solidification*, 2nd ed.; China Machine Press: Beijing, China, 2010; pp. 73–75.
26. Jo, S.M.; Kim, S.D.; Kim, T.-H.; Go, Y.; Yang, C.-W.; You, B.S.; Kim, Y.M. Sequential precipitation behavior of $Mg_{17}Al_{12}$ and Mg_2Sn in Mg-8Al-2Sn-1Zn alloys. *J. Alloys Compd.* **2018**, *749*, 794–802. [CrossRef]
27. Elsayed, F.R.; Sasaki, T.T.; Mendis, C.L.; Ohkubo, T.; Hono, K. Compositional optimization of Mg–Sn–Al alloys for higher age hardening response. *Mater. Sci. Eng. A* **2013**, *566*, 22–29. [CrossRef]
28. Kim, B.; Do, J.; Lee, S.; Park, I. In situ fracture observation and fracture toughness analysis of squeeze cast AZ51–xSn magnesium alloys. *Mater. Sci. Eng. A* **2010**, *527*, 6745–6757. [CrossRef]
29. Bu, F.; Yang, Q.; Guan, K.; Qiu, X.; Zhang, D.; Sun, W.; Zheng, T.; Cui, X.; Sun, S.; Tang, Z.; et al. Study on the mutual effect of La and Gd on microstructure and mechanical properties of Mg-Al-Zn extruded alloy. *J. Alloys Compd.* **2016**, *688*, 1241–1250. [CrossRef]
30. Cai, C.; Song, R.; Wen, E.; Wang, Y.; Li, J. Effect of microstructure evolution on tensile fracture behavior of Mg-2Zn-1Nd-0.6Zr alloy for biomedical applications. *Mater. Des.* **2019**, *182*, 108038. [CrossRef]
31. Fu, W.; Wang, R.H.; Xue, H.; Kuang, J.; Zhang, J.Y.; Liu, G.; Sun, J. Effects of Zr addition on the multi-scale second-phase particles and fracture behavior for Mg-3Gd-1Zn alloy. *J. Alloys Compd.* **2018**, *747*, 197–210. [CrossRef]